Check for updates

Cite this: *RSC Adv.*, 2023, **13**, 9402

Effect of morphological variation in three-dimensional multiwall carbon nanotubes as the host cathode material for high-performance rechargeable lithium–sulfur batteries†

Pashupati R. Adhikari, [a] Eunji Lee,[c] Lee Smith,[a] Jeongyong Kim, [c] Sheldon Shi [a] and Wonbong Choi [*ab]

Lithium–sulfur batteries (LSBs) demonstrate potential as next-generation energy storage systems due to the high theoretical capacity and energy density of the sulfur cathode (1672 mAh g^{-1} and 2600 W h kg^{-1}, respectively) in addition to the low-cost, natural abundance, and environmentally benign characteristics of sulfur. However, the insulating nature of sulfur requires an efficient conductive and porous host material such as three-dimensional carbon nanotubes (3D CNTs). Identifying parameters that provide high conduction pathways and short diffusion lengths for Li-ions within the CNT structure is essential for a highly efficient CNT-S cathode in a LSB. Herein, the effect of morphological variation in 3D CNTs as a sulfur host material is studied, and parameters that affect the performance of a CNT-S cathode in LSB are investigated. Four different 3D CNTs are synthesized *via* the chemical vapor deposition (CVD) technique that vary in specific surface area (SSA), CNT diameter, pore sizes, and porosity. The superior 3D CNT-S (CNT-S-50) cathode, which possessed high surface area and porosity as compared to the rest of the 3D CNT-S cathodes, with ∼38 wt% (6.27 mg cm^{-2}) sulfur loading, demonstrated an areal and specific discharge capacity of 8.70 mAh cm^{-2} and 1387 mAh g^{-1} at 0.1C, respectively. Results from this work demonstrate that the combination of high surface area and porosity are two crucial parameters in 3D CNTs as an efficient sulfur host material for LSB cathodes.

1. Introduction

Rechargeable lithium-ion batteries (LIBs) based on the lithium insertion-type electrode materials such as lithium metal oxide (*e.g.*, LiCoO$_2$) or lithium metal phosphate (*e.g.* LiFePO$_4$) as a cathode and graphite or other carbon materials as an anode are approaching their theoretical energy density limits.[1,2] On the other hand, the demand for electrical energy storage (EES) is steadily increasing with the development of advanced portable electronic devices, electrical vehicles (EVs), and large-scale energy storage systems to stabilize the grid and balance the renewable energy supply demand.[3–5] Therefore, there is an urgent need to develop a next-generation high-energy-density battery system beyond the electrochemical insertion mechanism to meet the growing demand. In recent years, lithium–

sulfur batteries (LSBs) have drawn increasing research interest as one of the most promising candidates for next-generation EES. Sulfur as an active cathode material in LSBs is highly advantageous because of its natural abundance, low cost, and environmentally benign characteristics.[6–9] LSBs can approach a high theoretical specific capacity of 1672 mAh g^{-1} and gravimetric energy density of 2600 Wh kg^{-1}, outperforming the capacity and the energy density of conventional LIBs, ∼250 mAh g^{-1} and ∼800 Wh kg^{-1}, respectively.[10,11] In practice, however, the specific energy of LSBs needs to be enhanced for them to be considered as the next generation of EES. One of the approaches to enhance the specific energy (E_g) in LSBs is by increasing the active material (sulfur) loading amount as given in eqn (1).

$$E_g = \frac{V m_A C}{\sum W_i} \tag{1}$$

where V is the average cell operating voltage, m_A is the active material loading (g cm^{-2}), C is the specific capacity of the active material (mAh g^{-1}), and W_i is the weight of individual cell components (g cm^{-2}). To achieve high energy density and cycling performance, the design of a cathode structure having high sulfur loading and its full utilization is critical. Such

[a]*Department of Mechanical Engineering, University of North Texas, 3940 North Elm St, Denton, TX 76207, USA. E-mail: wonbong.choi@unt.edu*

[b]*Department of Material Science and Engineering, University of North Texas, 3940 North Elm St., Denton, TX 76207, USA*

[c]*Department of Energy Science, Sungkyunkwan University, Suwon 16419, Republic of Korea*

† Electronic supplementary information (ESI) available. See DOI: https://doi.org/10.1039/d3ra00502j

a design is also critical because the voltage of LSBs ($\sim$2.3 V) is much lower compared to LIBs ($\sim$3.6 V).[12–14] Higher sulfur loading and its full utilization is feasible with a conductive network possessing high surface area and porosity such that it provides high conduction pathways and short diffusion lengths for Li-ions within the structure for optimum performance of the LSB.

Despite promising theoretical implications, several rather severe obstacles hinder the practical application of LSBs. Primarily these issues are associated with the electrochemistry of LSBs that becomes more prominent with increasing sulfur loading, leading to capacity fading and low cyclic stability. Elemental sulfur in itself is highly insulating (5×10^{-30} S cm^{-1} at room temperature), and its discharge products (Li$_2$S/Li$_2$S$_2$) lead to a low active material utilization and poor cycling performance.[15] The intrinsic issues of LSB, such as significant volume change of sulfur particles during cycling, the dissolution of polysulfide intermediates into the electrolyte, and their shuttling from one electrode to another across the separator, further contribute to the loss of active materials, low coulombic efficiency, and poor cycle life. Continuous shuttling of the polysulfides from the cathode side to the anode side causes dendrite growth on the lithium surface, potentially puncturing the separator and ultimately leading to cell failure. Therefore, many efforts have been devoted over the years to improving the electrochemical performance of carbon-sulfur (C/S) composite cathodes for LSBs.[16–19] Various cathode designs in which sulfur is confined within the conductive frameworks, such as conductive polymer,[20,21] metal compounds,[22–24] and carbon with various morphologies, including porous carbon materials,[25–30] carbon nanotubes,[31–33] carbon nanofibers,[34,35] and graphene oxides,[36–38] have been studied. These designs have tremendously improved the electrochemical performance of the LSBs by enhancing the conductivity of the sulfur composite and preventing the dissolution and shuttling of the polysulfide intermediates. However, multi-step fabrication methods for the cathode designs discussed above are complicated and involve addition of binding and additive materials, such as PVDF and carbon black (super P), in addition to solvent with sulfur, increasing the overall weight of the cathode material. In contrast, free standing and binder free 3D CNTs involve a simple, cost-effective, and facile synthesis approach, where 3D CNTs can be directly used as a current collector and conductive scaffold allowing high loading amounts of sulfur due to their high surface area. Although, 3D CNTs have been shown to demonstrate superior performances in LSB cathodes, how their morphological variation affects the polysulfide chemistry and cathode performance in LSBs has never been studied before and requires an in-depth understanding. The primary motivation of this work is to gain an in-depth understanding of the role of various morphological parameters of the 3D CNTs and identify the ones that are most critical for an efficient CNT-S cathode in high-performance LSB.

Herein, we investigate how morphological variation in 3D-CNT affects cathode performance and demonstrate that the combination of porosity and the surface area available within the CNT matrix are primarily the crucial parameters that dictate the overall performance of the CNT-S composite cathode in LSB. We fabricated binder-free composite cathodes using 3D CNTs of varying morphological parameters and elemental sulfur with different configurations. The morphological parameters of the 3D CNTs are analyzed and investigated in terms of physical and electrochemical characterization to identify the superior 3D CNTs. The investigation revealed that the superior 3D CNTs provide an efficient electron channel for effective sulfur utilization due to sufficient surface area and porosity, which promote electrolyte absorbability and confine polysulfides for better cell performance. The superior 3D CNT-S (CNT-S-50) cathode, which possessed high surface area and porosity as compared to the rest of the 3D CNT-S cathodes, with $\sim$38 wt% ($\sim$6.27 mg cm^{-2}) of sulfur loading, demonstrated an areal and specific discharge capacity of 8.70 mAh cm^{-2} and 1387 mAh g^{-1} at 0.1C, respectively. The results from this work have shown that the combination of high surface area and porosity are crucial parameters in 3D CNTs as an efficient sulfur host material for LSB cathode.

2. Experimental design

2.1. Fabrication of 3D CNT-S cathodes

3D CNT-S composite cathode fabrication began with DC sputtering of titanium (Ti) metal as a supporting layer and nickel (Ni) as a catalyst layer on channeled Cu-mesh of 50 μm thickness and 65 μm hole size (TMP Inc). Cu mesh was cut into 1 cm × 1 cm, mechanically pressed under 100 MPa of pressure to flatten the surface for uniformity, washed with acetone, rinsed thoroughly with deionized water, and vacuum dried at 60 °C for 20 minutes to completely evaporate the moisture. Deposition of Ti and Ni layers was carried out by DC magnetron sputtering (Desktop Pro, Denton vacuum) at room temperature and 5 mTorr of deposition pressure under argon plasma. The Ti deposition time was kept constant at 8 minutes and the Ni deposition times were varied within the range of 6–12 minutes with 2 minutes step to achieve varying catalyst thickness that would ultimately determine the overall CNT morphology. To determine the film deposition rate, two additional samples of Si-wafer with a portion of them covered with Kapton tape (later removed to create a step for thickness measurement) were also sputtered during Ti and Ni deposition. Ti and Ni thicknesses on Si-wafer were measured using an atomic force microscope (AFM) and individual deposition rates (nm min^{-1}) were determined. Table S1† summarizes the deposition rate and total thickness of both Ti and Ni on Cu-mesh used for CNT synthesis.

The 3D CNTs, herein referred to as CNTs, were synthesized by CVD (Firstnano CVD Inc.) on the Ti and Ni deposited Cu-mesh as a substrate under the stoichiometric gas mixture of 1 : 2 volume ratio of H$_2$: C$_2$H$_4$ for 30 minutes in the temperature range of 650–700 °C using tip growth mechanism.[39] The CVD was purged with N$_2$ and Ar gas before, during, and after the CNTs synthesis process. A schematic showing the steps involved in the complete CNTs synthesis process is given in Fig. S1.† Using FeCl$_3$ as an etchant, Ni, Ti, and Cu were all etched away for $\sim$1 hour and thoroughly washed with deionized water to ensure the removal of all traces of the metals. The CNTs were

vacuum dried at 80 °C for 4 hours to evaporate the moisture completely. Four different CNTs were synthesized with varying diameter, SSA, pore sizes, and porosity, namely CNT-30, CNT-40, CNT-50, and CNT-60, where the two-digit numbers represent the Ni catalyst thickness in nanometers (nm). Corresponding CNT-S cathodes were fabricated, namely CNT-S-30, CNT-S-40, CNT-S-50, and CNT-S-60, respectively, by coating sulfur powder (99.9% Sigma Aldrich Inc.) onto the CNTs. The CNTs with uniformly coated sulfur were hot-pressed at 155 °C for 25 minutes to ensure complete sulfur diffusion into the CNT matrix, followed by drying under vacuum at 60 °C for 24 h. Sulfur content for each cathode (CNT-S-30, CNT-S-40, CNT-S-50, and CNT-S-60) was kept at ∼40 wt% as a controlled parameter for comparison. For the optimized CNT-S cathode (CNT-S-50), the S-content was ∼38 percent.

2.2. Material characterization

The surface area properties of the CNTs were characterized using a Micromeretics 3Flex surface characterization device (3Flex, Micromeritics, Norcross, GA) by adsorption isotherm technique, also known as Brunauer–Emmett–Teller (BET) isotherm. The CNTs were first placed inside the sample test tubes, where they were initially degassed and dried to remove any moisture in the CNTs. This process was carried out at a temperature of 200 °C for 24 hours. Once degassed, the test tubes were depressurized with nitrogen gas and attached to the 3-Flex characterization device. Once the test tubes were in place, they were vacuumed and lowered into a vat of liquid nitrogen to execute the adsorption and desorption processes. Nitrogen gas was pumped in and out of the test tubes. Sequentially, the samples' adsorption and desorption were measured to determine the SSA, pore sizes, and porosity. This form of characterization recorded the BET surface area, Barrett–Joyner–Halenda (BJH) pore volume, and density functional theory (DFT) measurements of the CNTs. In addition, relevant characteristics such as SSA, pore sizes, porosity, and adsorption with respect to relative pressure were obtained and analyzed. Nitrogen adsorption–desorption isotherm plots showing the quantity adsorbed ($cm^3 g^{-1}$ STP) with respect to relative pressure (P_0/P) for all four CNT samples are given in Fig. S2(a–d†). In the figure, the BET isotherms for each CNT sample show complete desorption of the adsorbed nitrogen gas, indicating mesoporous CNT structures.

Apart from BET isotherm characterization, the diameters of the CNTs were determined from the scanning electron microscopy (SEM) images obtained using field emission scanning electron microscopy (JEOL-JSM-7001F). Raman spectroscopy was performed on all four CNT samples using a commercial Confocal Raman Spectrometer (Alpha-300S, WiTec Instrument GmbH). A 532 nm wavelength unpolarized laser was used for Raman excitation to avoid the polarization effect of the CNTs. The Raman scattered signal was filtered through an edge filter, then dispersed by a spectrometer having 600 grooves per mm grating for one second of exposure time. Likewise, one of the CNT-S (CNT-S-50) cathode morphology was characterized by using FEI Nova-NanoSEM 230T. The SEM was

fitted with an energy-dispersive X-ray spectroscopy (EDS) detector (EDAX, Model: Apollo X). Prior to scanning, the detector was calibrated using pure Ni standard and the raw data was processed using EDAX's Genesis Spectrum version 6.0 software. X-ray diffraction (XRD) patterns (Rigaku III Ultima) were scanned at a scan rate of 1° min^{-1} using a step size of 0.05° within 2θ range of 10–70° using CuKα radiation (1.54 Å) throughout the θ–2θ mode.

2.3. Coin cell fabrication and electrochemical characterization

CR2032-coin cells (Welcos Ltd.) were used to assemble the Li–S coin cells. Cell assembly was performed inside an argon-filled glove box (MBraun, Inc. Germany) by constantly maintaining humidity (H_2O) and oxygen (O_2) concentrations below 0.5 ppm level. The 3D CNT-S composite and bare Li metal (thickness of 120 μm) were used as cathode and anode, respectively. The conventional LSB electrolyte that includes lithium bis-trifluoromethanesulphonylimide (1 M LiTFSI, 99% Sigma Aldrich) and lithium nitrate (0.25 M $LiNO_3$, 99.99%, Sigma Aldrich) salt in the organic solvent of 1,2-dimethoxyethane (DME, 99.5%, Sigma Aldrich) and 1,3-dioxolane (DOL, 99%, Sigma Aldrich) with 1 : 1 volumetric ratio was prepared and used as an electrolyte with electrolyte-to-sulfur (E/S) ratio of ∼10 : 1 (μL of electrolyte : mg of S). Typically, $LiNO_3$ is used as an additive for lithium surface passivation. The monolayer polypropylene (PP) separator Celgard 2400 (Welcose Ltd.) with a thickness of 25 μm was used as a separator to isolate two electrically conducting electrodes, the CNT-S cathode and the bare Li-metal anode. Coin cells were assembled for all four CNT-S cathodes and rested for 24 hours before being tested and characterized.

The electrochemical performances of all four CNT-S cathodes in coin cells were evaluated in a multi-channel battery testing unit (MACCOR-series 4000). The C-rate tests of each cell were performed at 0.05C, 0.1C, 0.5C, 0.75C, 1.0C, 2.0C, and back to 0.5C for 5 cycles each. The current required to charge and discharge at various C-rates was calculated based on the sulfur loading amount (current, A = theoretical capacity (mAh g^{-1}) × C-rate (per hour) × S-mass in mg). Galvanostatic charge–discharge (GCD) tests were carried out at room temperature within a voltage range of 1.7–2.8 V. Cyclic voltammetry (CV) for each cell was performed by applying a linearly swept potential at a scan rate of 0.05 mV s^{-1} and measuring the resultant current response using CH electrochemical workstation. Similarly, electrochemical impedance spectroscopy (EIS) measurements were performed within the frequency range of 10^6–0.01 Hz with an AC perturbation of 5 mV, also using the CH electrochemical workstation.

3. Results and discussions

3.1. Structural characterization of CNT-S cathode

SEM images of all four CNT samples were taken using a field-emission scanning electron microscope (FE SEM) to estimate the diameters and analyze the overall CNT structures. Fig. 1(a–
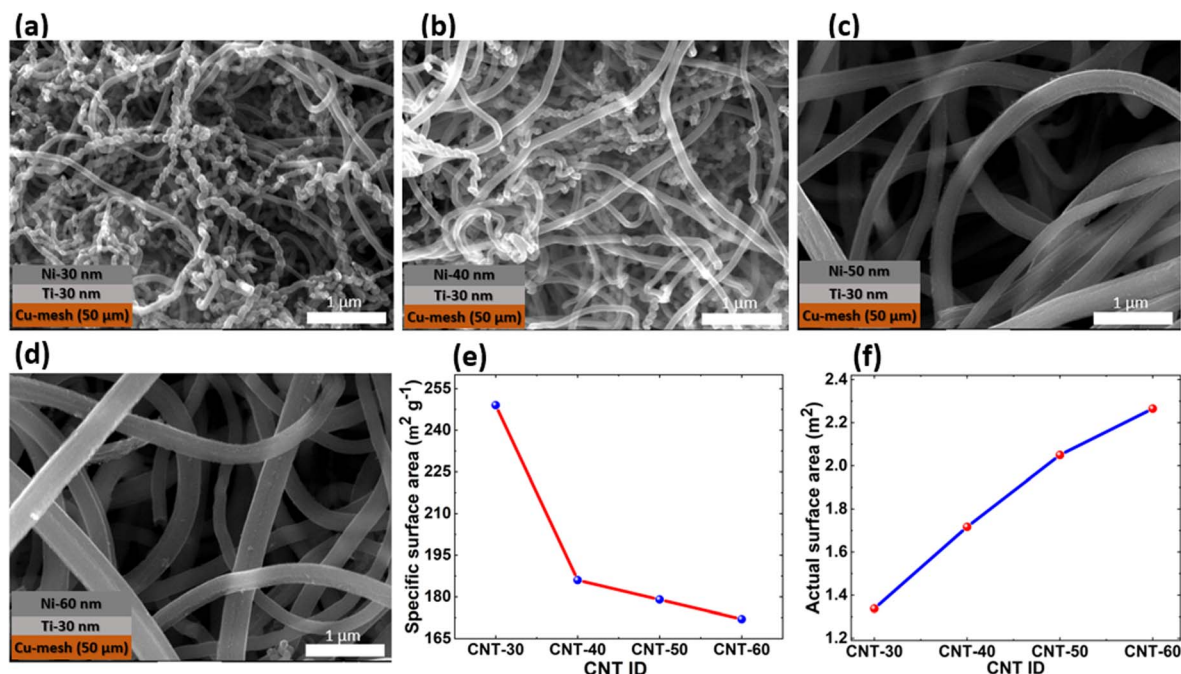
Fig. 1 SEM images of (a) CNT-30, (b) CNT-40, (c) CNT-50, (d) CNT-60, (e) specific surface area (SSA) the CNTs, and (f) actual surface area of the CNTs based on their corresponding masses.

d) show the SEM images of CNT-30, CNT-40, CNT-50, and CNT-60, respectively, along with corresponding Ti and Ni layer thicknesses on the Cu mesh used in the synthesis. Each CNT sample's diameter measurement was repeated three times and the average diameter was determined with standard deviation. CNT diameters ranged between ~95 nm for CNT-30 to ~405 nm for CNT-60, where the SSA increased with decreasing CNTs diameter.[40] Various input parameters during the CNT synthesis contribute to its morphology changes. CNT diameter is proportional to the catalyst thickness, while the length and the areal density are proportional to the CNT growth time. Fig. 1(e) shows the SSA of all four CNT samples from the BET characterization that ranged between 172.07 m^2 g^{-1} and 248.57 m^2 g^{-1}. The areal density of the CNTs was in the range of ~5.4 mg cm^{-2} to 13.1 mg cm^{-2}. Although the SSA decreases with increasing CNTs diameter, the actual surface area increases with increasing CNTs diameter, as shown in Fig. 1(f), due to increasing areal density. From the BET results, it was also revealed that the pore size distribution ranged between 5.55 and 12.6 nm indicating mesoporous CNTs structure. The surface area and porosity of CNTs play an essential role in mobilizing electrons and ions that facilitate polysulfide conversion during cycling. The porosities of each CNT sample were calculated using the T-plot analysis. The mesopore volume was determined by subtracting the micropore volume from the total pore volume, which was then stated as a proportion of the total pore volume to reflect the porosity percentage.[41] The porosities of the CNTs ranged between 11.05 and 18.71 percent, as shown in Fig. S3.†

CVD-grown free-standing CNTs and its corresponding low-magnification SEM image are shown in Fig. 2(a). The

fabrication of CNT-S cathode that involved the uniform distribution of elemental sulfur over the free-standing CNTs and mechanical hot press at 155 °C allowing the sulfur particles to melt and infuse into the CNTs network, is illustrated in Fig. 2(b). The interconnected CNTs provide a large surface area and narrow pore size distribution. A low magnification SEM image of one of the CNT-S cathodes (CNT-S-50) is shown in Fig. 2(c) along with EDS elemental maps of C and S showing the uniform distribution of sulfur within the conductive network of CNTs as shown in Fig. 2(d) and (e), respectively. The EDS spectrum showing the C and S peaks in the CNT-S cathode is shown in Fig. 2(f).

To further support these results, XRD characterization (Rigaku III Ultima) was performed. As shown in Fig. 3(a), all peak positions of the CNT-S cathode correspond to the standard orthorhombic crystal structure of sulfur in Fig. 3(b). The XRD pattern of CNTs shown in Fig. 3(c) has two prominent peaks related to graphitic hexagonal carbon at (002) and (101) with 2θ at 26.05° and 44.35°, respectively. Raman spectra of all four CNT samples are shown in Fig. 3(d), including their D-band and G-band, along with corresponding I_D/I_G ratios. All CNT samples show similar features with the D band at 1350 cm^{-1} and the G band at 1590 cm^{-1}. The D band corresponds to a hybridized vibrational mode associated with grain edges, which indicates the presence of some disorder in the structure. The G band is related to an in-plane vibrational mode of bond stretching between two atoms in a graphene unit cell.[36] A disordered structure with a low degree of graphitization is relatively more favorable for efficient Li transport during charging and discharging compared to highly crystalline graphite.[37,38] The ratio of intensity related to defects (I_D) to intensity related to in-plane
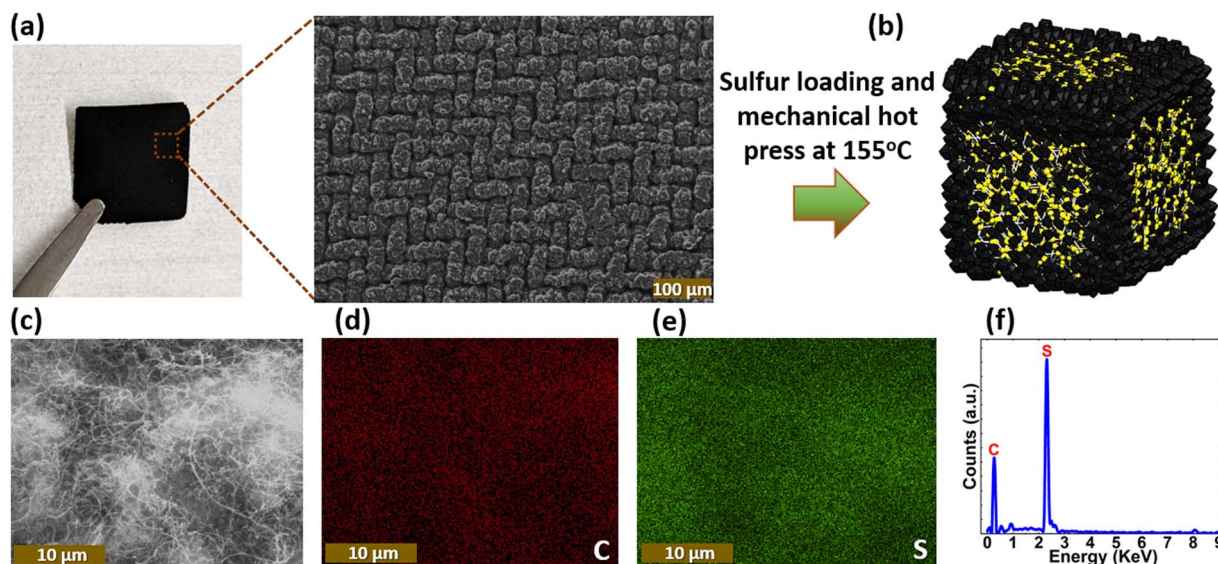
Fig. 2 Fabrication and characterization of CNT–S cathode structure: (a) CVD-grown CNTs along with its low magnification SEM image. (b) Schematic illustration showing uniform coating of sulfur onto the CNTs resulting in CNT–S cathode after mechanical hot press at ~155 °C. (c) Low magnification SEM image of CNT–S (CNT-S-50) cathode. (d) EDS mapping of carbon on the CNT–S cathode. (e) EDS mapping of sulfur on the CNT–S cathode. (f) EDX spectrum of the CNT–S cathode from SEM image in (c).
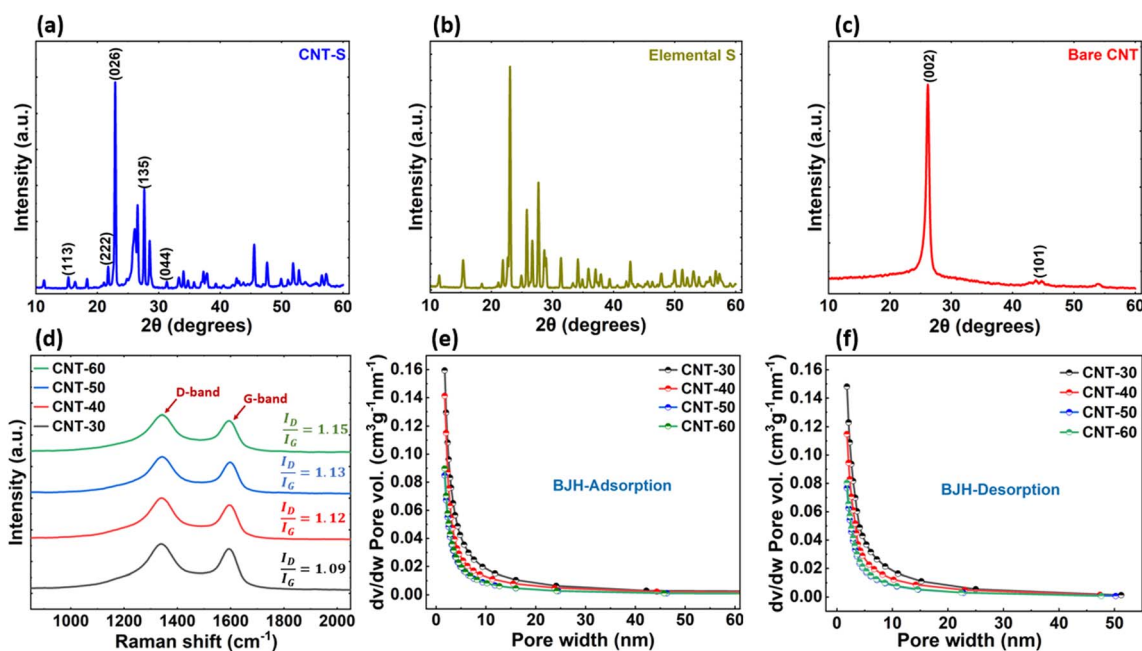

Fig. 3 Structural characterization of CNT–S cathode: (a) XRD patterns of CNT–S cathode, (b) XRD patterns of elemental sulfur, (c) XRD patterns of as-synthesized bare CNTs, (d) Raman spectroscopy of all four CNTs showing the characteristic D and G-band peaks and their corresponding I_D/I_G ratios, (e) BJH adsorption pore size distribution curves of CNTs, and (f) BJH desorption pore size distribution curves of CNTs.

vibration (I_G) for all the CNTs were greater than 1.0, implying that they are highly defective graphite structures, consistent with the broad peak observed at $2\theta = 26.05°$. A summary of the ratios, along with CNT diameters with standard deviation, is given in Table 1.

In addition, to further understand the morphology of the CNTs in terms of pore volume and pore size distribution, we analyzed the Barrett–Joyner–Halenda (BJH) adsorption and desorption behavior of the 3D CNTs from the BET measurements as shown in Fig. 3(e) and (f), respectively. From this analysis, we observed that even though all CNTs have uniform and narrow pore size distribution, CNT-50 has the smallest pore volume (0.0848 cm^3 g^{-1} nm^{-1} for adsorption and 0.0767 cm^3 g^{-1} nm^{-1} for desorption) of all the CNTs, therefore offering

Table 1 3D CNTs with corresponding CNT diameter and I_D/I_G

CNT ID	CNT diameter (nm)	Standard deviation (nm)	I_D/I_G
CNT-30	95	8	1.09
CNT-40	135	7	1.12
CNT-50	350	13	1.13
CNT-60	405	11	1.15

a better morphology for Li-ion diffusion and constraint volume expansion during cycling of the LSBs demonstrating better battery performance than others. A complete summary of the pore size distribution of all four CNTs are given in Table S2† for comparison.

3.2. Li–S cell performance

LSBs of all four CNT-S cathodes were subjected to electro-chemical performance testing to analyze the electrochemical kinetics of the CNT-S cathodes. CV tests were performed in the voltage range of 1.7–2.7 V vs. Li^+/Li at a low scan rate of 0.05 mV s^{-1}. CV curves of all four CNT-S cells clearly show all anodic and cathodic peaks, as shown in Fig. 4(a). The reduction peaks in LSBs based on CNT-S cathodes occur at around 2.3 and 2.0 V. The reduction peak at 2.3 V corresponds to the reduction of sulfur to long-chain polysulfides (Li_2S_x, $3 \geq x \geq 8$) and the second peak at 2.0 V corresponds to the conversion of long-chain to short-chain polysulfides (Li_2S_2 and Li_2S).

Similarly, in an anodic scan, the adjacent oxidation peak at ~2.3 and ~2.4 V corresponds to the conversion of lithium sulfides (Li_2S/Li_2S_2) to higher-order polysulfides and then to

sulfur (S_8). However, the peaks of CNT-S-30 and CNT-S-40 have a significant shift and are less sharp than those of CNT-S-50 and CNT-S-60, indicating inefficient Li-ion transfer and poor LiPS conversion. Among all four Li–S cells, CNT-S-50 exhibited the highest reduction potential and the lowest oxidation potential, indicating fast redox kinetics and high reversibility, which could primarily be attributed to the high surface area, the highest porosity (Fig. S3†), and the smaller pore size distribution. Even though a dense electrode with low porosity is sometimes desired to minimize electrolyte intake and parasitic weight of the cathode in LSB, it requires higher surface area and porosity to allow higher sulfur loading and its full utilization.[11,26] The porosity significantly enhances electrochemical performance as the combination of electrolyte access and short diffusion path lengths for both electronic and Li-ion transport provides a beneficial microstructure for Li-ion insertion/extraction.[42] Likewise, the high surface area and porosity combination enhance Li-ion transport and active material utilization by efficient LiPS conversion kinetics.[43] The high surface area and the highest porosity in CNT-S-50 provide efficient electrolyte access and short diffusion path lengths (higher diffusion coefficient) for electronic and Li-ion transport, demonstrating the best electrochemical performance. The reduction peak at around 2.0 V of the CNT-S-50 cell significantly shifts to a higher potential than other cells suggesting enhanced conversion from LiPSs to Li_2S. In the oxidation process, the CNT-S-50 cell also shows the lowest oxidation potential, revealing that the oxidation of Li_2S is also enhanced, avoiding the formation of dead sulfur. The shape of the CV curve remains sharp and tall for the CNT-S-50 cell compared to the rest of the cells, demonstrating a steady and reversible
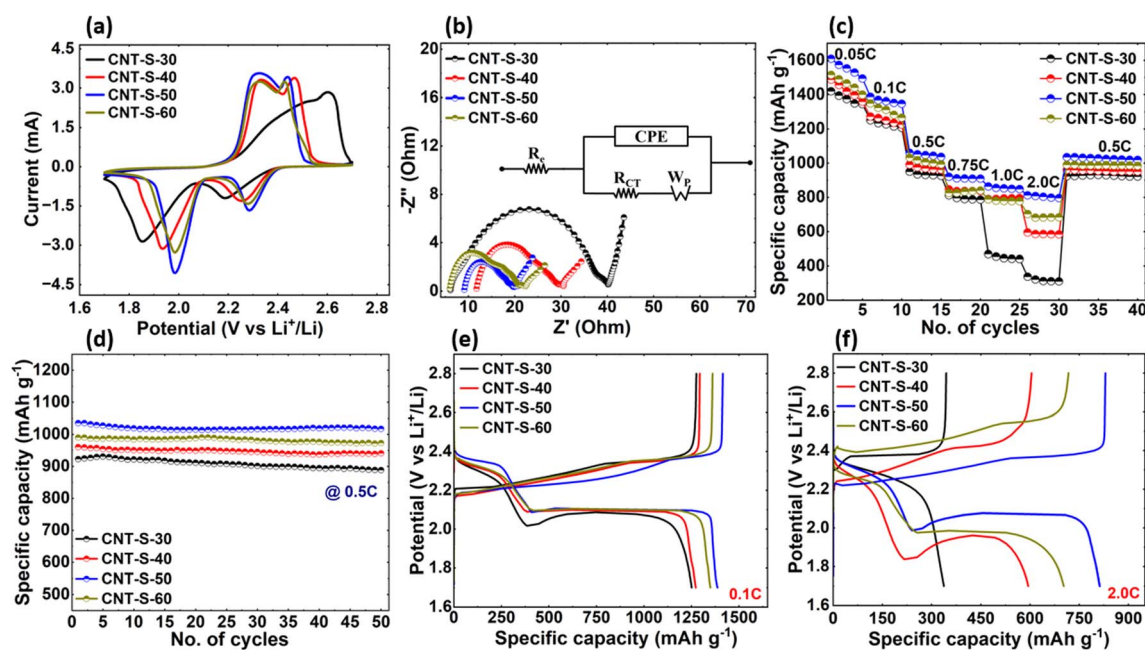

Fig. 4 Electrochemical performance of Li–S cells: (a) cyclic voltammetry (CV) tests at a scan rate of 0.05 mV s^{-1}. (b) Electrochemical impedance spectroscopy (EIS) within a frequency range of 10^6–0.01 Hz. (c) Specific capacity versus the number of cycles at different C-rates. (d) Cyclic stability performance at 0.5C for the first 50 cycles. (e) Galvanostatic charge–discharge profiles at 0.1C. (f) Galvanostatic charge–discharge profiles at 2.0C.

electrochemical reaction of sulfur by efficient ion-charge accessibility and improved confinement of polysulfides within the CNT-S cathode structure.

Additionally, the EIS was performed in the frequency range of 10^6–0.01 Hz to evaluate internal and charge transfer resistance of all four CNT-S cells in the initial condition, as shown in Fig. 4(b). The Nyquist plot for all the CNT-S cells consists of a semicircle in the high to medium frequency range and an inclined slope in the lower frequency range. The diameter of the semicircle corresponds to charge-transfer resistance (R_{CT}), as shown in the equivalent circuit model in the inset. CNT-S-50 cell showed the lowest impedance of 21.1 Ω. In contrast, the impedances of CNT-S-30, CNT-S-40, and CNT-S-60 cells were 40.15 Ω, 30.91 Ω, and 23.48 Ω, respectively, which is in good agreement with the CV curves of the cells as to why CNT-S-50 has the lowest impedance. It is also noted that the impedance increased with decreasing CNT diameter with the exception of CNT-S-60, which had a higher impedance than that of CNT-S-50. In general, the R_{CT} and the overall impedance of CNT-S cathodes are much lower than that of other metal-based electrodes.[44]

As shown in Fig. 4(c), all the Li–S cells were discharged and charged at various C-rates (0.05C, 0.1C, 0.5C, 0.75C, 1.0C, 2.0C, and back to 0.5C) and were evaluated. The CNT-S-30 showed poor performance among all the cells, particularly at high C-rates. In contrast, the CNT-S-50 cell exhibited the optimum performance, indicating good agreement with the CV and EIS results, which suggests that the CNT-S-50 structure is highly stable at high C-rates due to the possession of the high surface area and porosity, allowing an efficient LiPS conversion and faster Li-ion diffusion. Furthermore, the CNT-S-50 cell demonstrated that even at a higher C-rate (2.0C), the cell could deliver a reversible specific capacity of 812 mAh g^{-1}. When the rate was returned to 0.5C, the discharge capacity was maintained at 1036 mAh g^{-1} (capacity retention of ~98%).

In order to further validate the individual C-rate performance of all the cells for a longer cycle, the cyclic stability tests of all the CNT-S cells were evaluated at 0.5C rate for further 50 cycles, as shown in Fig. 4(d). While all CNT-S cells exhibited good cyclic stability, the CNT-S-50 cell exhibited superior performance, which is in good agreement with the CV, the EIS, and the C-rate test results already discussed. For the first 50 cycles at 0.5C current, the CNT-S-30, CNT-S-40, CNT-S-50, and CNT-S-60 cathodes delivered ~923, 960, 1036, and 990 mAh g^{-1} of discharge capacity, which are 55%, 57%, 62%, and 59% of the theoretical capacity of sulfur (1672 mAh g^{-1}), respectively. After 50 cycles, the retention rates were 96.2%, 97.9%, 98.2%, and 98.2%, respectively.

Galvanostatic charge–discharge (GCD) profiles of all four Li–S cells at 0.1C were evaluated (Fig. 4(e)). The CNT-S-50 cell showed the lowest polarization overpotential of 150 mV, indicating the fast conversion kinetics. In contrast, the polarization overpotentials of CNT-S-30, CNT-S-40, and CNT-S-60 cells at 0.1C were 220 mV, 180 mV, and 180 mV, respectively, which are also in good agreement with all the electrochemical performances of the cells discussed above. Furthermore, the GCD profiles of the CNT-S-50 at a high C-rate of 2.0C, as shown in

Fig. 4(f), exhibited a remarkable performance with a low polarization overpotential of 250 mV. In contrast, the polarization overpotentials of CNT-S-30, CNT-S-40, and CNT-S-60 cells at 2.0C were 120 mV, 480 mV, and 480 mV, respectively. The 120 mV polarization overpotential of CNT-S-30 at a 2.0C rate is incomparable to the other cells due to its one-step LiPS conversion resulting in a very low specific capacity. Interfacial impedance in a LSBs has a direct impact on how the cell performs. Higher impedance has higher tendency to block an efficient transport of electrons and ions leading to poor redox kinetics. We found that the change of impedance in cathode has more influence on the cell performance particularly at higher C-rate.

To summarize the comparative discussion presented above in a meaningful perspective and highlight the reasons why certain CNT-S cathodes performed better than others, we put forth the following analogy: The weights of the CNTs are in order: CNT-30 (5.37 mg cm^{-2}), CNT-40 (9.23 mg cm^{-2}), CNT-50 (11.45 mg cm^{-2}), and CNT-60 (13.17 mg cm^{-2}). As such, the actual surface area (m^2) possessed by each of the CNTs are in order: CNT-30 (1.33 m^2), CNT-40 (1.72 m^2), CNT-50 (2.05 m^2), and CNT-60 (2.27 m^2) based on the individual weight of the corresponding CNTs (Fig. 1(f)). Note that the areal density of the CNTs (mg cm^{-2}) increases with increasing CNT diameter and CNT length. In a similar context, the porosities of the CNTs (Fig. S3†) are in order: CNT-30 (13.31%), CNT-40 (11.05%), CNT-50 (18.71%), and CNT-60 (13.69%). With respect to the actual surface area of the CNTs, the results are mostly consistent with the electrochemical performance of the cells in that the higher the surface area, the better the rate and cyclic performance, except for CNT-S-60. CNT-S-50 has a slightly lower surface area than CNT-S-60 (~10 percent less surface area) but shows better cell performance. In this case, the higher porosity of CNT-S-50 (~27 percent) contributes more to better cell performance than the higher actual surface area of CNT-S-60 (~10 percent). Mainly, for CNT-S-50, a combination of the much higher porosity of all the CNTs and the high actual surface area contribute to the best cell performance and is thereby chosen as the optimized CNT-S cathode in this work.

The same trend does not hold when comparing CNT-S-40 and CNT-S-30. The porosity of CNT-40 is less than that of CNT-30 (~17 percent less porosity) and the actual surface area of CNT-40 is much higher than that of CNT-30 (~29 percent higher). In this case, however, the higher actual surface area of CNT-S-40 results in better cell performance compared to that of CNT-S-30. Based on the analogy, we determine that there is a collective contribution of the porosity and the actual surface area of the CNTs in the CNT-S cathodes toward the overall LSB performance.

To further evaluate the cyclic performance and stability of the CNT-S-50 cathode, CV scans were performed at a low scan rate of 0.05 mV s^{-1} for the first five cycles to verify the superior electrochemical kinetics, as shown in Fig. 5(a). From the figure, it is evident that all the first five cycles are sharp and tall in both cathodic and anodic peaks with excellent retention, indicating highly efficient electrochemical kinetics and high sulfur utilization. Fig. 5(b) shows the specific capacity *versus* the number of
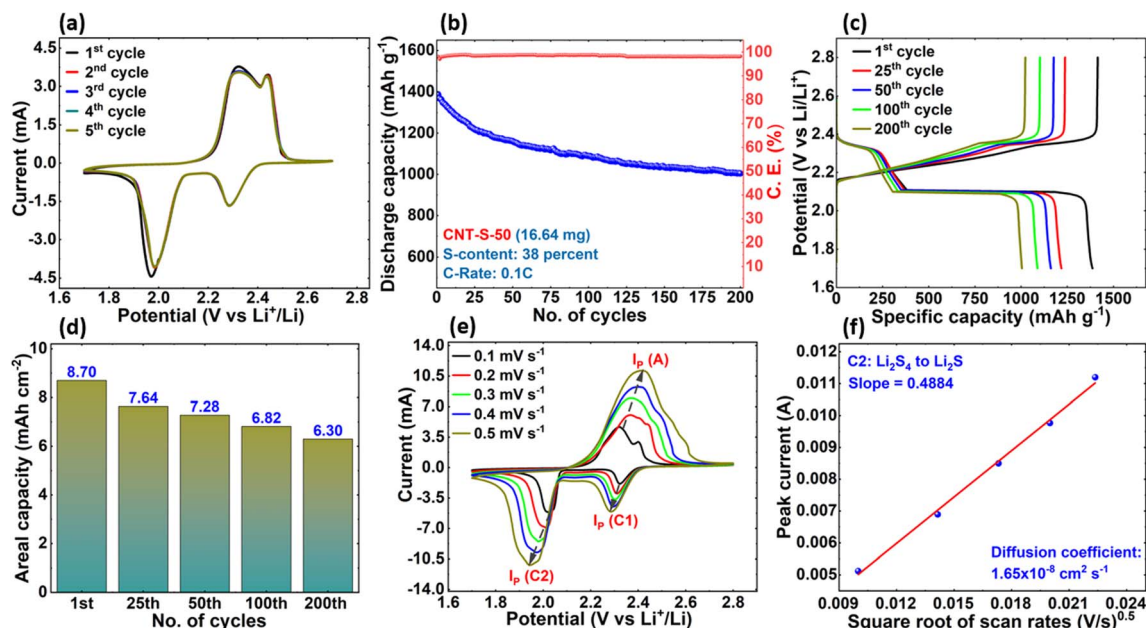
Open Access Article. Published on 22 March 2023. Downloaded on 8/2/2025 8:48:20 PM. This article is licensed under a Creative Commons Attribution-NonCommercial 3.0 Unported Licence.

Fig. 5 Electrochemical performance of CNT-S-50 LSB: (a) CV curves at a scan rate of 0.05 mV s^{-1}. (b) Cyclic stability performance at 0.1C rate with coulombic efficiency (CE%). (c) Galvanostatic charge–discharge profiles of different cycles at 0.1C. (d) The number of cycles *vs.* areal capacity for different cycles at 0.1C. (e) CV curves measured at various scan rates. (f) The plot of CV peak currents *versus* the square root of scan rate for the cathodic reaction of Li$_2$S$_4$ to Li$_2$S.

cycles of the CNT-S-50 cell for the first 200 cycles. The cell delivered an initial discharge capacity of 1387 mAh g^{-1} at 0.1C, with coulombic efficiency of greater than 98% for the first 200 cycles. A noticeable capacity decay is observed in the first few cycles due to polysulfide formation and its shuttling leading to the loss of sulfur, which is unavoidable.[44] During the initial charge–discharge cycling, soluble polysulfide species move freely through the separator to the Li-anode and multiple concurrently parasitic reactions occur simultaneously. For example, the soluble polysulfide species can react with Li-ions in the electrolyte and generate insoluble Li$_2$S. This reaction consumes electrolytes and causes rapid capacity fading, particularly in the first few cycles. In addition, the soluble species may react with the Li-metal and form insoluble Li$_2$S$_2$ and Li$_2$S. Both Li$_2$S$_2$ and Li$_2$S easily precipitate onto the Li-anode surfaces. Moreover, these nonconductive Li$_2$S$_2$–Li$_2$S can continue to react with the soluble species and form more short-chain soluble species causing capacity fading. After the first few cycles, the redox kinetics significantly stabilize, reducing the capacity fading for stable cycling.

The galvanostatic charge–discharge (GCD) profiles of the CNT-S-50 cell at 0.1C, as shown in Fig. 5(c), exhibit two plateaus in the discharge profile at ∼2.3 and ∼2.0 V, while two plateaus are observed at ∼2.3 and ∼2.4 V in the charge profile, respectively. These results are in good agreement with CV curves involving reduction and oxidation reactions of the carbon-based sulfur cathode in LSBs.[45–47] The problem of continuous lithium erosion is compounded with the dissolved polysulfides that also get involved in the passivation film formation.[46,47] On the other hand, uncontrolled lithium dendrite formation is the main reason for the failure of LSBs.[48] Typically, the CNT-S cathode modified/

treated with catalysts such as MoS$_2$ or MoWS$_2$ in LSBs significantly improves redox kinetics and slows down LiPS dissolution, preventing shuttling of the LiPS and therefore exhibiting superior performance as compared to bare CNT-S cathode.[49,50] Even without modification, such as CNT/Catalyst (CNT/MoS$_2$ or CNT/MoWS$_2$), the CNT-S-50 cell performed comparatively well with 1386 mAh g^{-1} of specific capacity at 0.1C. On this front, if the optimized CNT-S cathode from this work (CNT-S-50) is modified with catalysts such as MoS$_2$ or MoWS$_2$, it could demonstrate a promising cell performance with longer cycle life and stability.

The areal capacity of the CNT-S-50 cell was also evaluated and is presented in Fig. 5(d). The areal capacity was 8.70 mAh cm^{-2} in the first cycle. At the 200th cycle, the areal capacity was 6.30 mAh cm^{-2} showing high areal capacity retention of over 72 percent. Due to the high surface area, narrow pore size distribution, and porosity, our CNTs have an advantage over many other carbon materials as the sulfur host material in the LSB cathode. With respect to areal capacity from this work, we have achieved one of the highest reported areal capacities in LSBs using as-synthesized CNTs as the sulfur host material.[51–56] Furthermore, the specific energy density of the CNT-S-50 cell reached 1097 Wh kg^{-1}, considering total cathode and active material weight, which could be further improved with higher sulfur content, ensuring the CNT possesses high surface area and porosity. The high surface area and pore volume of the CNTs synthesized in our lab have the advantage of providing short ionic paths and sufficient volume for electrolyte infiltration as an ion channel and hence can possess a high areal capacity.[12,13]

As we stated, the 3D CNTs appear to have provided efficient electrical pathways and short diffusion lengths (high diffusion

coefficient) for Li-ions, demonstrating high sulfur loading capability. While concluding that the CNT-S-50 is the optimized CNT-S cathode in this work, we calculated diffusion coefficients of all three conversion peaks of the CNT-S-50 Li–S cell during cycling (Cathodic-1, Cathodic-2, and Anodic). The diffusion coefficient of lithium-ion can be calculated based on the classical Randles–Sevcik equation, as given in eqn (2),[57,58]

$$I_p = 2.69 \times 10^5 n^{1.5} A D^{0.5} C V^{0.5} \qquad (2)$$

where I_P is the peak current, n is the number of electrons transferred during the reaction, which is 2 for LSBs, A is the active electrode area, D is the diffusion coefficient of lithium-ion in the unit of cm^2 s^{-1}, C is the concentration of lithium-ion in the electrolyte in the unit of mol mL^{-1}, and v is the scan rate in the unit of V s^{-1}. CV analyses at various scan rates were carried out to determine the diffusion coefficient of lithium-ion. The CV was performed on the CNT-S-50 cell at different scan rates ranging from 0.1 mv s^{-1} to 0.5 mv s^{-1}. Fig. 5(e) shows conversion peaks for the cathodic reaction of S_8 to Li_2S_4 (peak C1), the cathodic reaction of Li_2S_4 to Li_2S (peak C2), and the anodic reaction of Li_2S to S_8 (peak A). As shown in Fig. 5(f), the peak currents increase with increasing scan rate. All the cathodic and anodic peak currents are linear with the square root of the scan rate, indicating that the reactions are diffusion-controlled.[42] The diffusion coefficient for I_P (C2) was calculated, which shows a high diffusion coefficient (short diffusion length) compared to many literature that have reported high-performance LSBs with modified CNT-S cathode.[49,58–61] The diffusion coefficients of other reaction types are also calculated and summarized in Table S3 in the ESI.†

4. Conclusion

The effect of morphological variation in 3D CNTs as a sulfur host material in LSB cathode towards battery performance was demonstrated. Parameters that contribute to enhancing redox kinetics in LSBs enabling ion-movement pathways for efficient charge–discharge cycles, were identified. Primarily, these parameters were surface area, porosity, and pore size distribution, directly affecting the cell impedance. High surface area and porosity in 3D CNTs have provided efficient electrical pathways and short diffusion lengths for Li-ions while demonstrating high sulfur loading capability. By performing a series of material and electrochemical characterizations of four different 3D CNTs with varying morphology and their corresponding CNT-S cathodes, a superior CNT-S cathode was identified. The superior 3D CNT-S (CNT-S-50) cathode, which possessed high surface area and porosity as compared to the rest of the CNT-S cathodes, with ~38 wt% (6.27 mg cm^{-2}) of sulfur loading, demonstrated an areal and specific discharge capacity of 8.70 mAh cm^{-2} and 1387 mAh g^{-1} at 0.1C, respectively. This work opens up an avenue for further studying other porous and high surface area carbon materials as efficient sulfur host materials for LSBs of the future.

Conflicts of interest

There are no conflicts to declare.

Acknowledgements

References

1 N. Nitta, F. Wu, J. T. Lee and G. Yushin, Li-ion battery materials: present and future, *Mater. Today*, 2015, **18**, 252–264, DOI: 10.1016/j.mattod.2014.10.040.

2 K. M. Abraham, Prospects and Limits of Energy Storage in Batteries, *J. Phys. Chem. Lett.*, 2015, **6**, 830–844, DOI: 10.1021/jz5026273.

3 J. B. Goodenough and K.-S. Park, The Li-Ion Rechargeable Battery: A Perspective, *J. Am. Chem. Soc.*, 2013, **135**, 1167–1176, DOI: 10.1021/ja3091438.

4 M. Armand and J.-M. Tarascon, Building better batteries, *Nature*, 2008, **451**, 652–657, DOI: 10.1038/451652a.

5 V. Etacheri, R. Marom, R. Elazari, G. Salitra and D. Aurbach, Challenges in the development of advanced Li-ion batteries: a review, *Energy Environ. Sci.*, 2011, **4**, 3243–3262, DOI: 10.1039/C1EE01598B.

6 F. Pei, L. Lin, A. Fu, S. Mo, D. Ou, X. Fang and N. Zheng, A Two-Dimensional Porous Carbon-Modified Separator for High-Energy-Density Li-S Batteries, *Joule*, 2018, **2**, 323–336, DOI: 10.1016/j.joule.2017.12.003.

7 M. A. Pope and I. A. Aksay, Structural Design of Cathodes for Li-S Batteries, *Adv. Energy Mater.*, 2015, **5**, 1500124, DOI: 10.1002/aenm.201500124.

8 X. Ji and L. F. Nazar, Advances in Li-S Batteries, *J. Mater. Chem.*, 2010, **20**, 9821–9826, DOI: 10.1039/b925751a.

9 M.-K. Song, Y. Zhang and E. J. Cairns, A Long-Life, High-Rate Lithium–Sulfur Cell: A Multifaceted Approach to Enhancing Cell Performance, *Nano Lett.*, 2013, **13**, 5891–5899, DOI: 10.1021/nl402793z.

10 Y.-T. Liu, S. Liu, G.-R. Li, T.-Y. Yan and X.-P. Gao, High Volumetric Energy Density Sulfur Cathode with Heavy and Catalytic Metal Oxide Host for Lithium–Sulfur Battery, *Adv. Sci.*, 2020, **7**, 1903693, DOI: 10.1002/advs.201903693.

11 A. Manthiram, Y. Fu and Y.-S. Su, Challenges and Prospects of Lithium–Sulfur Batteries, *Acc. Chem. Res.*, 2013, **46**, 1125–1134, DOI: 10.1021/ar300179v.

12 E. Cha, M. D. Patel, J. Park, J. Hwang, V. Prasad, K. Cho and W. Choi, 2D MoS_2 as an efficient protective layer for lithium metal anodes in high-performance Li-S Batteries, *Nat. Nanotechnol.*, 2018, **13**, 337–344, DOI: 10.1038/s41565-018-0061-y.

13 M. D. Patel, E. Cha, C. Kang, B. Gwalani and W. Choi, High performance rechargeable Li-S Batteries using binder-free large sulfur-loaded three-dimensional carbon nanotubes, *Carbon*, 2017, **118**, 120–126, DOI: 10.1016/j.carbon.2017.03.035.

14 J. H. Lee, C. S. Yoon, J.-Y. Hwang, S.-J. Kim, F. Maglia, P. Lamp, S.-T. Myung and Y.-K. Sun, High-energy-density lithium-ion battery using a carbon-nanotube-Si composite anode and a compositionally graded $Li[Ni_{0.85}Co_{0.05}Mn_{0.10}]$

O$_2$ cathode, *Energy Environ. Sci.*, 2016, **9**, 2152–2158, DOI: **10.1039/c6ee01134a**.

15 Y. Li, H. Zhan, S. Liu, K. Huang and Y. Zhou, Electrochemical properties of the soluble reduction products in rechargeable Li-S Battery, *J. Power Sources*, 2010, **195**, 2945–2949, DOI: **10.1016/j.jpowsour.2009.11.004**.

16 Z. Bian, T. Yuan, Y. Xu, Y. Pang, H. Yao, J. Li, J. Yang and S. Zheng, Boosting Li-S Battery by Rational Design of Freestanding Cathode with Enriched Anchoring and Catalytic N-Sites Carbonaceous Host, *Carbon*, 2019, **150**, 216–223, DOI: **10.1016/j.carbon.2019.05.022**.

17 J. Guo, Y. Xu and C. Wang, Sulfur-Impregnated Disordered Carbon Nanotubes Cathode for Lithium–Sulfur Batteries, *Nano Lett.*, 2011, **11**, 4288–4294, DOI: **10.1021/nl202297p**.

18 C. Song, Z. Bian, Y. Xu, Y. Pang, C. Peng and S. Zheng, High-Performance Li-S Battery Cathode Enabled by Immobilizing Sulfur in Hybrid Janus Host with Hierarchical Structure, *Mater. Lett.*, 2019, **249**, 173–176, DOI: **10.1016/j.matlet.2019.04.089**.

19 S. Zheng, P. Han, Z. Han, H. Zhang, Z. Tang and J. Yang, High Performance C/S Composite Cathodes with Conventional Carbonate-Based Electrolytes in Li-S Battery, *Sci. Rep.*, 2014, **4**, 4842, DOI: **10.1038/srep04842**.

20 M. Wang, W. Wang, A. Wang, K. Yuan, L. Miao, X. Zhang, Y. Huang, Z. Yu and J. Qiu, A multi-core-shell structured composite cathode material with a conductive polymer network for Li-S Batteries, *Chem. Commun.*, 2013, **49**, 10263–10265, DOI: **10.1039/c3cc45412f**.

21 B. H. Jeon, J. H. Yeon, K. M. Kim and I. J. Chung, Preparation and electrochemical properties of lithium–sulfur polymer batteries, *J. Power Sources*, 2002, **109**, 89–97, DOI: **10.1016/S0378-7753(02)00050-2**.

22 Z. W. She, W. Li, J. J. Cha, G. Zheng, Y. Yang, M. T. McDowell, P.-C. Hsu and Y. Cui, Sulphur-TiO$_2$ yolk-shell nanoarchitecture with internal void space for long-cycle lithium–sulphur batteries, *Nat. Commun.*, 2013, **4**, 1331, DOI: **10.1038/ncomms2327**.

23 X. Tao, J. Wang, C. Liu, H. Wang, H. Yao, G. Zheng, Z. W. Seh, Q. Cai, W. Li, G. Zhou, C. Zu and Y. Cui, Balancing surface adsorption and diffusion of lithium-polysulfides on nonconductive oxides for lithium–sulfur battery design, *Nat. Commun.*, 2016, **7**, 11203, DOI: **10.1038/ncomms11203**.

24 Y. Peng, B. Li, Y. Wang, X. He, J. Huang and J. Zhao, Prussian Blue: A Potential Material to Improve the Electrochemical Performance of Lithium–Sulfur Batteries, *ACS Appl. Mater. Interfaces*, 2017, **9**, 4397–4403, DOI: **10.1021/acsami.6b06890**.

25 N. Jayaprakash, J. Shen, S. S. Moganty, A. Corona and L. A. Archer, Porous Hollow Carbon@Sulfur Composites for High-Power Lithium–Sulfur Batteries, *Angew. Chem., Int. Ed.*, 2011, **50**, 5904–5908, DOI: **10.1002/anie.201100637**.

26 C. Zhang, H. B. Wu, C. Yuan, Z. Guo and X. W. Lou, Confining Sulfur in Double-Shelled Hollow Carbon Spheres for Lithium–Sulfur Batteries, *Angew. Chem., Int. Ed.*, 2012, **51**, 9592–9595, DOI: **10.1002/anie.201205292**.

27 L. Zhang, H. Huang, Y. Xia, C. Liang, W. Zhang, J. Luo, Y. Gan, J. Zhang, X. Tao and H. J. Fan, High-content of sulfur uniformly embedded in mesoporous carbon: a new electrodeposition synthesis and an outstanding lithium–sulfur battery cathode, *J. Mater. Chem. A*, 2017, **5**, 5905–5911, DOI: **10.1039/c7ta00328e**.

28 X. Li, X. Cheng, M. Gao, D. Ren, Y. Liu, Z. Guo, C. Shang, L. Sun and H. Pan, Amylose-Derived Macrohollow Core and Microporous Shell Carbon Spheres as Sulfur Host for Superior Lithium–Sulfur Battery Cathodes, *ACS Appl. Mater. Interfaces*, 2017, **9**, 10717–10729, DOI: **10.1021/acsami.7b00672**.

29 J. Song, T. Xu, M. L. Gordin, P. Zhu, D. Lv, Y.-B. Jiang, Y. Chen, Y. Duan and D. Wang, Nitrogen-Doped Mesoporous Carbon Promoted Chemical Adsorption of Sulfur and Fabrication of High-Areal-Capacity Sulfur Cathode with Exceptional Cycling Stability for Lithium–Sulfur Batteries, *Adv. Funct. Mater.*, 2014, **24**, 1243–1250, DOI: **10.1002/adfm.201302631**.

30 F. Qin, X. Wang, K. Zhang, J. Fang, J. Li and Y. Lai, High areal capacity cathode and electrolyte reservoir render practical Li-S Batteries, *Nano Energy*, 2017, **38**, 137–146, DOI: **10.1016/j.nanoen.2017.05.037**.

31 L. Wang, Y. Zhao, M. L. Thomas and H. R. Byon, In Situ Synthesis of Bipyramidal Sulfur with 3D Carbon Nanotube Framework for Lithium–Sulfur Batteries, *Adv. Funct. Mater.*, 2014, **24**, 2248–2252, DOI: **10.1002/adfm.201302915**.

32 Q. Q. Wang, J. B. Huang, G. R. Li, Z. Lin, B. H. Liu and Z. P. Li, A facile and scalable method to prepare carbon nanotube-grafted-graphene for high performance Li-S Battery, *J. Power Sources*, 2017, **339**, 20–26, DOI: **10.1016/j.jpowsour.2016.11.038**.

33 C. Jin, W. Zhang, Z. Zhuang, J. Wang, H. Huang, Y. Gan, Y. Xia, C. Liang, J. Zhang and X. Tao, Enhanced sulfide chemisorption using boron and oxygen dually doped multi-walled carbon nanotubes for advanced lithium–sulfur batteries, *J. Mater. Chem. A*, 2017, **5**, 632–640, DOI: **10.1039/C6TA07620C**.

34 K. Fu, Y. Li, M. Dirican, C. Chen, Y. Lu, J. Zhu, Y. Li, P. D. Bradford and X. Zhang, Sulfur gradient-distributed CNF composite: a self-inhibiting cathode for binder-free lithium–sulfur batteries, *Chem. Commun.*, 2014, **50**, 10277–10280, DOI: **10.1039/C4CC04970E**.

35 Z. Tong, L. Huang, W. Lei, H. Zhang and S. Zhang, Carbon-containing electrospun nanofibers for lithium–sulfur battery: Current status and future directions, *J. Energy Chem.*, 2021, **54**, 254–273, DOI: **10.1016/j.jechem.2020.05.059**.

36 T. Yang, J. Xia, Z. Piao, L. Yang, S. Zhang, Y. Xing and G. Zhou, Graphene-Based Materials for Flexible Lithium–Sulfur Batteries, *ACS Nano*, 2021, **15**, 13901–13923, DOI: **10.1021/acsnano.1c03183**.

37 Z. Ma, L. Tao, D. Liu, Z. Li, Y. Zhang, Z. Liu, H. Liu, R. Chen, J. Huo and S. Wang, Ultrafine nano-sulfur particles anchored on *in situ* exfoliated graphene for lithium–sulfur batteries, *J. Mater. Chem. A*, 2017, **5**, 9412–9417, DOI: **10.1039/c7ta01981e**.

38 Z. Ma, X. Huang, Q. Jiang, J. Huo and S. Wang, Enhanced Cycling Stability of Lithium–Sulfur batteries by Electrostatic-Interaction, *Electrochim. Acta*, 2015, **182**, 884–890, DOI: 10.1016/j.electacta.2015.10.009.

39 M. A. Azam, N. S. A. Manaf, E. Talib and M. S. A. Bistamam, Aligned carbon nanotube from catalytic chemical vapor deposition technique for energy storage device: a review, *Ionics*, 2013, **19**, 1455–1476, DOI: 10.1007/s11581-013-0979-x.

40 A. Peigney, Ch. Laurent, E. Flahaut, R. R. Bacsa and A. Rousset, Specific surface area of carbon nanotubes and bundles of carbon nanotubes, *Carbon*, 2001, **39**, 507–514, DOI: 10.1016/S0008-6223(00)00155-X.

41 B. Adeniran and R. Mokaya, Low temperature synthesized carbon nanotube superstructures with superior CO_2 and hydrogen storage capacity, *J. Mater. Chem. A*, 2015, **3**, 5148–5161, DOI: 10.1039/c4ta06539e.

42 T. Brezesinski, J. Wang, S. H. Tolbert and B. Dunn, Ordered mesoporous α-MoO3 with iso-oriented nanocrystalline walls for thin-film pseudocapacitors, *Nat. Mater.*, 2010, **9**, 146–151, DOI: 10.1038/nmat2612.

43 H. Zhang, L. K. Ono, G. Tong, Y. Liu and Y. Qi, Long-life lithium–sulfur batteries with high areal capacity based on coaxial CNTs@TiN-TiO$_2$ sponge, *Nat. Commun.*, 2021, **12**, 4738, DOI: 10.1038/s41467-021-24976-y.

44 N. Kang, Y. Lin, L. Yang, D. Lu, J. Xiao, Y. Qi and M. Cai, Cathode porosity is a missing key parameter to optimize lithium–sulfur battery energy density, *Nat. Commun.*, 2019, **10**, 4597, DOI: 10.1038/s41467-019-12542-6.

45 S. Moon, Y. H. Jung, W. K. Jung, D. S. Jung, J. W. Choi and D. K. Kim, Encapsulated Monoclinic Sulfur for Stable Cycling of Li-S Rechargeable Batteries, *Adv. Mater.*, 2013, **25**, 6547–6553, DOI: 10.1002/adma.201303166.

46 J. Zheng, M. Gu, H. Chen, P. Meduri, M. H. Engelhard, J.-G. Zhang, J. Liu and J. Xiao, Ionic liquid -enhanced solid-state electrolyte interface (SEI) for lithium–sulfur batteries, *J. Mater. Chem. A*, 2013, **1**, 8464–8470, DOI: 10.1039/c3ta11553d.

47 S. S. Zhang and J. A. Read, A new direction for the performance improvement of rechargeable lithium–sulfur batteries, *J. Power Sources*, 2012, **200**, 77–82, DOI: 10.1016/j.jpowsour.2011.10.076.

48 D. Aurbach, E. Zinigrad, H. Teller and P. Dan, Factors Which Limit the Cycle Life of Rechargeable Lithium (Metal) Batteries, *J. Electrochem. Soc.*, 2000, **147**, 1274, DOI: 10.1149/1.1393349.

49 S. Bhoyate, J. Kim, E. Lee, B. Park, E. Lee, J. Park, S.-H. Oh, J. Kim and W. Choi, Mixed Phase 2D Mo$_{0.5}$W$_{0.5}$S$_2$ Alloy as a Multi-Functional Electrocatalyst for a High-Performance Cathode in Li-S Batteries, *J. Mater. Chem. A*, 2020, **8**, 12436–12445, DOI: 10.1039/d0ta04354k.

50 S. Bhoyate, B. Park, S.-H. Oh and W. Choi, Defect Engineered MoWS Alloy Catalyst Boost the Polysulfide Conversion in Lithium–Sulfur Battery, *J. Power Sources*, 2021, **511**, 230426, DOI: 10.1016/j.jpowsour.2021.230426.

51 J. Li, W. Xie, S. Zhang, S.-M. Xu and M. Shao, Boosting the Rate Performance of Li–S Batteries under High Mass-Loading of Sulfur Based on a Hierarchical NCNT@Co-CoP Nanowire Integrated Electrode, *J. Mater. Chem. A*, 2021, **9**, 11151–11159, DOI: 10.1039/d1ta00959a.

52 X. Li, Y. Zhang, S. Wang, Y. Liu, Y. Ding, G. He, X. Jiang, W. Xiao and G. Yu, Scalable High-Areal-Capacity Li-S Batteries Enabled by Sandwich-Structured Hierarchically Porous Membranes with Intrinsic Polysulfide Adsorption, *Nano Lett.*, 2020, **20**, 6922–6929, DOI: 10.1021/acs.nanolett.0c03088.

53 Y. Lu, J.-L. Qin, T. Shen, Y.-F. Yu, K. Chen, Y.-Z. Hu, J.-N. Liang, M.-X. Gong, J.-J. Zhang and D.-L. Wang, Hypercrosslinked Polymerization Enabled N-Doped Carbon Confined Fe$_2$O$_3$ Facilitating Li Polysulfides Interface Conversion for Li-S Batteries, *Adv. Energy Mater.*, 2021, **11**, 2101780, DOI: 10.1002/aenm.202101780.

54 L. Su, J. Zhang, Y. Chen, W. Yang, J. Wang, Z. Ma, G. Shao and G. Wang, Cobalt-Embedded Hierarchically-Porous Hollow Carbon Microspheres as Multifunctional Confined Reactors for High-Loading Li-S Batteries, *Nano Energy*, 2021, **85**, 105981, DOI: 10.1016/j.nanoen.2021.105981.

55 R. Wang, R. Wu, C. Ding, Z. Chen, H. Xu, Y. Liu, J. Zhang, Y. Ha, B. Fei and H. Pan, Porous Carbon Architecture Assembled by Cross-Linked Carbon Leaves with Implanted Atomic Cobalt for High-Performance Li-S Batteries, *Nano-Micro Lett.*, 2021, **13**, 151, DOI: 10.1007/s40820-021-00676-6.

56 Q. Pang and L. F. Nazar, Long-Life and High-Areal-Capacity Li-S Batteries Enabled by a Light-Weight Polar Host with Intrinsic Polysulfide Adsorption, *ACS Nano*, 2016, **10**, 4111–4118, DOI: 10.1021/acsnano.5b07347.

57 P. Zhu, J. Zhu, J. Zang, C. Chen, Y. Lu, M. Jiang, C. Yan, M. Dirican, R. K. Selvan and X. Zhang, A Novel Bi-Functional Double-Layer RGO–PVDF/PVDF Composite Nanofiber Membrane Separator with Enhanced Thermal Stability and Effective Polysulfide Inhibition for High-Performance Lithium–Sulfur Batteries, *J. Mater. Chem. A*, 2017, **5**, 15096–15104, DOI: 10.1039/c7ta03301j.

58 Z. Liu, B. Liu, P. Guo, X. Shang, M. Lv, D. Liu and D. He, Enhanced Electrochemical Kinetics in Lithium–Sulfur Batteries by Using Carbon Nanofibers/Manganese Dioxide Composite as a Bifunctional Coating on Sulfur Cathode, *Electrochim. Acta*, 2018, **269**, 180–187, DOI: 10.1016/j.electacta.2018.02.160.

59 D. Guo, X. Li, W. Wahyudi, C. Li, A.-H. Emwas, M. N. Hedhili, Y. Li and Z. Lai, Electropolymerized Conjugated Microporous Nanoskin Regulating Polysulfide and Electrolyte for High-Energy Li-S Batteries, *ACS Nano*, 2020, **14**, 17163–17173, DOI: 10.1021/acsnano.0c06944.

60 G. Yang, R. Tao, C. J. Jafta, C. Shen, S. Zhao, L. He, L. Belharouak and J. Nanda, Investigating Multiscale Spatial Distribution of Sulfur in a CNT Scaffold and Its Impact on Li-S Cell Performance, *J. Phys. Chem. C*, 2021, **125**, 13146–13157, DOI: 10.1021/acs.jpcc.1c02288.

61 H. Wang, G. Yan, M. Li, H. Ji, Y. Feng, J. Shi and X. Zhang, Nucleophilic Ring-Opening of Thiolactones: A Facile Method for Sulfhydrylization of a Carbon Nanotube-Based Cathode toward High-Performance Li-S Batteries, *ACS Sustainable Chem. Eng.*, 2022, **10**(15), 5005–5014, DOI: 10.1021/acssuschemeng.2c00204.